Composite Structures 287 (2022) 115299

Contents lists available at ScienceDirect

Composite Structures

journal homepage: www.elsevier.com/locate/compstruct

A comprehensive investigation on macro–micro crack interactions in functionally graded materials using ordinary-state based peridynamics

M. Ozdemir [a,b,*], M. Imachi [c], S. Tanaka [d], S. Oterkus [a], E. Oterkus [a]

[a] Department of Naval Architecture, Ocean and Marine Engineering, University of Strathclyde, Glasgow, United Kingdom
[b] Department of Naval Architecture and Marine Engineering, Ordu University, Ordu, Turkey
[c] TechnoStar Co., Ltd., Tokyo, Japan
[d] Graduate School of Advanced Science and Engineering, Hiroshima University, Higashi-Hiroshima, Japan

ARTICLE INFO

Keywords:
Peridynamics
Functionally graded materials
Micro-cracks
Crack-speed

ABSTRACT

In the present work, interactions between a macro-crack and various micro-crack configurations are studied extensively. Influence of different micro-crack configurations on propagation of a main crack is numerically examined by ordinary state-based peridynamics. Certain micro-crack configurations improve toughness of the specimens, while the some only has marginal impact on the crack growth rate. Furthermore, very complex crack patterns are effectively simulated by the present implementation of ordinary state-based formulation.

1. Introduction

Functionally Graded Materials (FGMs) are considered to be advanced material types, which have become prevalent owing to the advancements in the additive manufacturing technologies [1]. Depending on the field of application, the material properties of a structure on one face can be adjusted for specific requirements, while the other face may have different properties. Furthermore, the fracture toughness of a material can be tailored so as to effectively control the crack initiation and propagation.

Randomly distributed micro-cracks in a solid may impact the apparent elastic properties of the body considerably [2]. On the other hand, crack propagation and stress field ahead of a crack tip in engineering materials can be controlled by the existence of micro-cracks [3–12] and holes [13–16]. Rubinstein [3] investigated the interaction between a co-linear micro-crack array and a semi-infinite macro crack in terms of the stress intensity factors (SIFs) and stress potentials. Kachanov [4] reported that a micro-crack array can significantly alter the stress concentration at the main crack tip. Hutchinsen [5] discussed how the micro-cracks affect the stress field ahead of a main crack tip, and investigated how arbitrarily oriented low-density micro-cracks act as a shield. Brencich and Carpinteri [6] modelled the micro-cracks in front of a main crack as a damage process zone, and the interactions between macro–micro cracks as well as micro–micro cracks were examined.

Petrova et al. [7] conducted a comprehensive literature survey involving macro–micro crack interactions for two-dimensional (2D) cases under tensile, shear and combined stress states. Ducourthial et al. [8] numerically studied influence of the micro-structure, i.e., micro-cracks, on the propagation of fatigue cracks in heterogeneous brittle materials. Feng et al. [9] carried out a numerical work addressing the interactions of a macro crack with a plenty of micro-cracks. The authors stated that their method can be utilized for predicting effective material properties of solids including uniform and non-uniform micro-cracks. Zhou et al. [10] employed Voronoi tessellation model to construct the micro-structure of ceramics, and investigated effects of the several parameters, e.g., grain size, grain boundary strength and micro-cracks on the crack propagation and toughness. Rahimi et al. [17] proposed a toughening mechanism for crack propagation in FGMs with sharp material interfaces. Their proposal involves two different approach: (i) putting softer material sub-region, (ii) flipped material properties in a certain sub-region, see [17] for details. Recently, multiple crack propagation and the toughening mechanisms with micro-cracks and holes have been addressed by employing extended finite element method (XFEM) [18–20] and phase-field method [14].

The superior properties of NURBS have been recognized and implemented in fracture parameter evaluation of FGM plates. Bhardwaj et al. [21] adopted extended Isogeometric Analysis (XIGA) for the SIF evaluation of FGM plates with first order shear deformation theory. Then, Singh et al. [22] employed generalized higher order shear deformation theory for calculation of fracture parameters in FGM plates. A series of comprehensive numerical works for various crack configurations, loading and boundary conditions, as well as the plate

* Corresponding author at: Department of Naval Architecture, Ocean and Marine Engineering, University of Strathclyde, Glasgow, United Kingdom.
E-mail addresses: murat.ozdemir@strath.ac.uk (M. Ozdemir), michiya.imachi@e-technostar.com (M. Imachi), satoyuki@hiroshima-u.ac.jp (S. Tanaka), selda.oterkus@strath.ac.uk (S. Oterkus), erkan.oterkus@strath.ac.uk (E. Oterkus).

https://doi.org/10.1016/j.compstruct.2022.115299
Received 31 August 2021; Received in revised form 12 January 2022; Accepted 22 January 2022
Available online 5 February 2022
0263-8223/© 2022 The Authors. Published by Elsevier Ltd. This is an open access article under the CC BY license (http://creativecommons.org/licenses/by/4.0/).

shapes were also carried out in [22]. Furthermore, Bhardwaj et al. [23] implemented XIGA for the FGMs with thermally induced cracks. The influence of flaws and inclusions on the SIFs was also investigated in the same work. A semi-homogenized XIGA approach for examining the effects of flaws and inclusions on the SIFs of central cracked FGMs was proposed in [24]. Apart from the fracture simulation of FGMs, Soni et al. [25] studied static bending of functionally graded carbon nanotube reinforced plates in the framework of inverse hyperbolic shear deformation theory.

The treatment of even a single crack in continuum media might be challenging due to the requirements of the special techniques in conventional methods. In recent times, Perdiynamics (PD) [26] was proposed with an excellent capability of handling discontinuities without any significant additional effort, as PD employs equation of motion in the form of integration, which is valid throughout entire domain regardless of discontinuities. The simplest form of PD formulation, the so called bond-based PD [27], establishes force interactions between material points (particles) in terms of relative deformation to each other, which brings about restrictions on Poisson's ratio. Unlike the bond-based PD, Ordinary State-Based (OSB) PD removes these restrictions by the definition of elaborated interactions between the particles [28].

These outstanding features of the PD have been recognized by researchers to investigate interactions between a macro crack and small sized defects, e.g., micro-cracks and holes. Vazic et al. [11] adopted the bond-based PD for simulating interactions between a macro-crack and a series of co-linear and parallel small cracks. It was shown that certain small crack configurations reduce the crack growth speed significantly. Then, Basoglu et al. [12] conducted a more comprehensive study for the modelling of micro-cracks as a toughening mechanism using the bond-based PD. Aside to the bond-based PD works, Rahimi et al. [15] and Karpenko et al. [16] adopted the OSB-PD to investigate toughening effects of the small-sized holes on propagation of a main crack.

Present study can be considered as follow-up of a series of the works conducted by the present authors. The 2D OSB-PD formulation proposed by Le et al. [29] was utilized for elastodynamics problems of cracked specimens to evaluate mixed-mode SIFs for stationary cracks [30], and fast propagating cracks [31]. Imachi et al. [31] introduced the transition bond concept to avoid the numerical oscillations caused by sudden release of the PD bonds between two particles. The crack arrest phenomenon was later simulated by the OSB-PD model and the transition bond concept [32]. It was reported that the transition bond concept has great importance for avoiding the premature arrest of cracks. The same OSB-PD formulation was implemented for dynamic fracture in FGMs by Ozdemir et al. [33]. In that paper, both fast crack propagation under tensile loading and three-point bending tests were considered. Crack branching and mix-mode crack propagation were captured as well. Recently, Imachi et al. [34] developed the smoothed variable horizon implementation for improving computational efficiency in elastodynamics problems, including SIFs evaluation.

To the best of authors' knowledge, micro-cracks interacting with a main crack in FGMs have not been modelled and simulated by PD yet, even though these interactions have been studied extensively for homogeneous materials, see [6,7,9,11,12]. Therefore, the main objective of the present work is to provide a comprehensive investigation and modelling framework for micro-crack and main crack interactions in FGMs for the first time in the literature. We employ the OSB-PD formulation, which was proposed by Le et al. [29] and later tailored by Ozdemir et al. [33] for FGMs.

The paper layout is organized as follows. We firstly describe fundamental equations of the 2D OSB-PD. Their numerical implementation involving the definition of PD parameters in FGMs is presented later. In the numerical examples, we initially validate our OSB-PD implementation for micro-cracks in homogeneous materials, whose results have been provided by Refs. [11,12]. After validating the present implementation, we consider fast crack growth scenarios in FGMs under tensile loading invoking various micro-crack configurations. Finally, three-point bending test scenarios of FGMs involving micro-cracks are modelled and studied numerically. In the end, we discuss the concluding remarks.

2. Fundamental equations

The OSB-PD formulation decouples the deviatoric and dilatational (volumetric) parts of the deformation state. Hence, the strain energy density and force states can be recovered in terms of the dilatational and deviatoric terms. Le et al. [29] derived the 2D OSB-PD formulation for both plane stress and strain conditions. In the present work, only the plane stress condition will be considered. Le et al. [29] proposed the PD strain energy density expression for a particle in a 2D solid body in the following form.

$$W = \frac{1}{2}\left(\kappa'\Theta^2 - \alpha(\underline{\omega e^{\mathrm{d}}}) \bullet \underline{e^{\mathrm{d}}}\right). \tag{1}$$

The PD parameters κ' and α in Eq. (1) can be evaluated from the correspondence of strain energy density and dilatation obtained by the PD and classical theory as:

$$\alpha = \frac{8\mu}{q}, \tag{2}$$

$$\kappa' = K + \frac{\mu(\nu+1)^2}{9(2\nu-1)^2}, \tag{3}$$

where K and μ are the bulk and shear moduli of the material. ν is the Poisson's ratio. The PD volume dilatation, Θ, for the plane stress case is defined as [29]:

$$\Theta = \beta\frac{(\underline{\omega\xi}) \bullet \underline{e}}{q}, \tag{4}$$

where $\beta = 2(2\nu-1)/(\nu-1)$. In Eqs. (1) and (4), the $(\bullet)$ operator stands for the dot product of two states as [28]:

$$\underline{\mathbf{A}} \bullet \underline{\mathbf{B}} = \int_{\mathcal{H}_{\mathbf{x}}} (\underline{\mathbf{AB}})\langle \mathbf{x}' - \mathbf{x}\rangle \mathrm{d}\mathcal{H}, \tag{5}$$

where $\langle\cdot\rangle$ involves the bond vector between two particles on which the PD states $\underline{\mathbf{A}}$ and $\underline{\mathbf{B}}$ operate. The elongation/shrinkage of a PD bond is represented by a scalar extension state $\underline{e} = |\mathbf{u}' - \mathbf{u}|$, and its deviatoric part is: $\underline{e^{\mathrm{d}}} = \underline{e} - (\Theta\underline{\xi})/3$. Accordingly, the bond vector for the undeformed configuration is expressed as $\boldsymbol{\xi} = \mathbf{x}' - \mathbf{x}$. The initial distance between the particles can be expressed by a scalar position state as $\underline{\xi} = |\boldsymbol{\xi}|$.

In the PD framework, the elastodynamics behaviour of a solid body is represented by the equation of motion in the integration form as [27]:

$$\rho(\mathbf{x})\ddot{\mathbf{u}}(\mathbf{x},t) = \int_{\mathcal{H}_{\mathbf{x}}} \left[\mathbf{f}(\mathbf{x},t) - \mathbf{f}'(\mathbf{x}',t)\right]\mathrm{d}\mathcal{H} + \mathbf{b}(\mathbf{x},t), \tag{6}$$

where $\mathbf{f}(\mathbf{x},t)$ defines the force density vector for the particle at $\mathbf{x}$ for any instance, t. By the same definition, the force density vector for the particle at $\mathbf{x}'$ is represented by $\mathbf{f}'(\mathbf{x}',t)$. The force density vectors are the outcome of the force states, which operate on the bond vector $\mathbf{x}' - \mathbf{x}$. The displacement vector is denoted by $\mathbf{u}$; the acceleration vector hence becomes $\ddot{\mathbf{u}}$. In the present form of the equation of motion, $\rho(\mathbf{x})$ stands for the location dependent material density, which can be set as variable for the modelling of FGMs. The neighbourhood of the particle at $\mathbf{x}$ is denoted by $\mathcal{H}_{\mathbf{x}}$, which will be called *horizon* hereafter. The horizon size is assumed to be constant in the present work, which means the number of particles within the horizon of each particle is the same, except for the boundary regions, which are truncated by the boundaries of a solid body. The horizon has a circular shape in 2D problems with a radius, δ. In Eqs. (2) and (4), the weighted volume of the horizon is represented by $q = (\underline{\omega\xi}) \bullet \underline{\xi}$. $\underline{\omega}$ is the scalar state of weight function, which is considered as linearly varying over the horizon, i.e, $\underline{\omega} = 1 - (\underline{\xi}/\delta)$. The body force density acting on the particle at $\mathbf{x}$ is $\mathbf{b}(\mathbf{x},t)$.

In the OSB-PD formulation, the force density vectors are aligned to the bond vector in the deformed configuration, but may have unequal magnitudes at each side of the bond. This is because, the force state of the particle at $\mathbf{x}$ due to interaction by the particle at $\mathbf{x}'$ is not only dependent on their relative deformation, but also the collective deformation of other particles within its horizon. In this regard, the force density vector for the particle located at $\mathbf{x}$ can be written as [29]:

$$\mathbf{f}(\mathbf{x},t) = f\mathbf{m}, \tag{7}$$

where $\mathbf{m}$ represents the unit bond vector in the deformed configuration, which is written as $\mathbf{m} = \boldsymbol{\eta}/|\boldsymbol{\eta}|$ with $\boldsymbol{\eta} = \mathbf{y}' - \mathbf{y}$. In this expression, $\mathbf{y}$ and $\mathbf{y}'$ stand for the position vectors in the deformed configuration for the particles initially located at $\mathbf{x}$ and $\mathbf{x}'$ points, respectively. The magnitude of the force density vector, f, for the plane stress condition is then given as [29]:

$$f = \beta\left(\kappa'\Theta - \frac{\alpha}{3}(\underline{\omega e^{\mathrm{d}}}) \bullet \underline{\xi}\right)\frac{\underline{\omega\xi}}{q} + \alpha\underline{\omega e^{\mathrm{d}}}. \tag{8}$$

The parameter q in Eqs. (4) and (8) plays a significant role to reduce the softening of the material near the boundaries because of the truncated horizon, since q is the denominator of both the force magnitude and the PD dilatation expressions. In a truncated horizon, q value becomes smaller than its correspondent for a horizon in bulk. Hence, the softening of the PD material near the boundaries can be compensated by the reduced value of the denominator in the force density and dilatation expressions [35].

2.1. Damage representation

In the PD perspective, the damage model is rather straightforward compared to the conventional continuum mechanics based methods. To model a damage or crack surface, the PD interactions passing through the damage area or crack surface can be removed. In this case, the scalar influence function must be multiplied by a step function, $\phi(\mathbf{x},\xi,t)$, which represents the bond condition for the particle at $\mathbf{x}$ and the associated bond vector ξ. If the bond is intact, the function takes the value of 1.0, otherwise it becomes zero. This simple implementation is valid regardless of the crack size; however, the discretization size as well as the horizon radius must be adjusted sufficiently small to accurately model the sharp micro-crack surfaces by this technique.

After proper modelling of the initial cracks, various failure criteria can be employed. Dipasquale et al. [36] discussed the advantages and disadvantages of various criteria applicable in the OSB-PD framework. These criteria are based on the critical stretch of a bond [37] and the maximum strain energy that can be stored in a bond [38]. In addition, Karpenko et al. [39] carried out a comprehensive investigation on the elimination of PD interactions in the OSB-PD framework invoking critical stretch based failure. Even though both critical stretch and maximum strain energy approaches perform quite well, the implementation of the critical stretch approach is more straightforward and has been widely considered thus far. We therefore adopt critical stretch based failure criteria given by Madenci and Oterkus [37] for evaluation of the crack propagation as:

$$s_{cr} = \sqrt{\frac{G_c}{\left(\frac{6}{\pi}\mu + \frac{16}{9\pi^2}(K-2\mu)\right)\delta}}. \tag{9}$$

If the stretch value of a bond obtained by Eq. (10) exceeds the critical stretch value by Eq. (9), the step function, $\phi(\mathbf{x},\xi,t)$, must be set to zero for the associated bond.

$$s = \frac{|\boldsymbol{\eta}| - |\xi|}{|\xi|}. \tag{10}$$

In Eq. (9), G_c is the critical energy release rate, which can be defined within the linear elastic fracture mechanics framework for the plane stress case as $G_c = K_{\mathrm{IC}}^2/E$, in which K_{IC} is the fracture toughness. It must be noted that the critical energy release rate has to be obtained in a point-wise manner in FGM modelling.

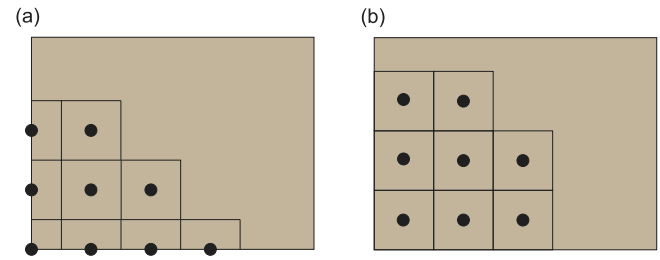

Fig. 1. Discretization schemes for PD domains: (a) particles are located along the boundaries, (b) particles are located with a distance from the boundaries.

For tracing the crack propagation as well as the damage accumulation, a scalar local damage parameter is utilized as [27]:

$$\varphi(\mathbf{x},t) = 1 - \frac{\int_{\mathcal{H}_{\mathbf{x}}} \phi(\mathbf{x},\xi,t)d\mathcal{H}}{\int_{\mathcal{H}_{\mathbf{x}}} d\mathcal{H}}. \tag{11}$$

The local damage parameter given in Eq. (11) represents the internal damage of a particle. Introducing an internal damage to a particle can be considered as one of the efficient ways to simulate the reduction in stiffness of the entire body. By adjusting this parameter, porosity [40, 41] and other micro-structural properties can be effectively introduced to a solid body.

The minimum local damage parameter, $\varphi(\boldsymbol{x},t)$, of a particle located on a crack surface may vary from 0.35 to 0.5 depending on the ratio of the horizon size to the particle distance. As an optimistic approach, it is assumed that a crack-tip advances to a new particle when the local damage parameter of that particle reaches the value of 0.5 [37].

3. Numerical solution of PD equations

The problem domain can be discretized as similar to conventional meshfree methods. In one discretization scheme as shown in Fig. 1(a), the particles are allocated along the boundaries of the problem domain. In this scheme, however, the particles on the boundaries would have truncated volumes unlike the particles in the bulk. We, therefore, employ the another discretization scheme shown in Fig. 1(b), so that the particles are allocated at the centre of the full grid cells and all particles have the same volume regardless of their location.

By discretizing a continuous problem domain, one can rewrite the continuous integral equations by means of summation of the discrete terms. In that sense, the equation of motion for the particle (k) can be expressed in discretized form as:

$$\rho_{(k)}\ddot{\mathbf{u}}_{(k)} = \sum_{j=1}^{N_{\mathcal{H}_k}} (\mathbf{f}_{(k)(j)} - \mathbf{f}_{(j)(k)})V'_{(j)} + \mathbf{b}_{(k)}. \tag{12}$$

The force density vectors $\mathbf{f}_{(k)(j)}$ and $\mathbf{f}_{(j)(k)}$ arise due to the interactions between the particles (k) and (j). $N_{\mathcal{H}_k}$ denotes the total number of particles within the neighbourhood of particle (k). The body force density vector acting on the point of interest is denoted by $\mathbf{b}_{(k)}$. At this point, it is worth mentioning that the traction forces are modelled as the body forces of the relevant particles in the solution of Eq. (12). The particle (j) within the horizon has a finite volume $V'_{(j)}$. If the boundary of horizon, $\mathcal{H}_k$, involves the entire volume of (j), $V'_{(j)}$ is taken as the full volume; otherwise, the volume correction procedure should be implemented to mitigate the errors caused by the numerical integration [37].

The acceleration term $\ddot{\mathbf{u}}_{(k)}$ in Eq. (12) can be simply obtained by dividing the both sides to the density of the particle, $\rho_{(k)}$. Then, the explicit central difference time integration scheme is employed to retrieve the velocity and displacement values.

In order to be able to solve Eq. (12), the magnitude of the force density vector, given in Eq. (8), is expressed in discretized form as:

$$f_{(k)(j)} = \beta\left(\kappa'_{(k)(j)}\Theta_{(k)} - \frac{\alpha_{(k)(j)}}{3}\sum_{j=1}^{N_{\mathcal{H}_k}}\phi_{(k)(j)}\underline{\omega}_{(k)(j)}\underline{e}^{\mathrm{d}}_{(k)(j)}\underline{\xi}_{(k)(j)}V'_{(j)}\right) \times \frac{\phi_{(k)(j)}\underline{\omega}_{(k)(j)}\underline{\xi}_{(k)(j)}}{q_{(k)}} + \alpha_{(k)(j)}\phi_{(k)(j)}\underline{\omega}_{(k)(j)}\underline{e}^{\mathrm{d}}_{(k)(j)}, \tag{13}$$

where the PD dilatation term in discretized form for the plane stress condition can be written as:

$$\Theta_{(k)} = \frac{\beta\sum_{j=1}^{N_{\mathcal{H}_k}}\phi_{(k)(j)}\underline{\omega}_{(k)(j)}\underline{\xi}_{(k)(j)}\underline{e}^{d}_{(k)(j)}V'_{(j)}}{q_{(k)}}. \tag{14}$$

In Eqs. (13) and (14), the term $q_{(k)}$ is independent of the material properties and it depends only the weight function, bond condition and the horizon of the particle (k), which is given as:

$$q_{(k)} = \sum_{j=1}^{N_{\mathcal{H}_k}}\phi_{(k)(j)}\underline{\omega}_{(k)(j)}\underline{\xi}_{(k)(j)}\underline{\xi}_{(k)(j)}V'_{(j)}. \tag{15}$$

Once the displacement values of the particles have been obtained by the explicit time integration, the stretch value between the particles within the neighbourhood of each other can be obtained as:

$$s_{(k)(j)} = \frac{|\boldsymbol{\eta}_{(k)(j)}| - |\boldsymbol{\xi}_{(k)(j)}|}{|\boldsymbol{\xi}_{(k)(j)}|}, \tag{16}$$

where $\boldsymbol{\eta}_{(k)(j)} = \mathbf{y}_{(j)} - \mathbf{y}_{(k)}$ and $\boldsymbol{\xi}_{(k)(j)} = \mathbf{x}_{(j)} - \mathbf{x}_{(k)}$. The stretch value, from Eq. (16), is then compared with the critical stretch value in Eq. (9) to assess whether the bond is intact or broken. Ultimately, the local damage parameter for the particle (k) can be expressed in discretized form for any instance as:

$$\varphi_{(k)} = 1 - \frac{\sum_{j=1}^{N_{\mathcal{H}_k}}\phi_{(k)(j)}V'_{(j)}}{\sum_{j=1}^{N_{\mathcal{H}_k}}V'_{(j)}}. \tag{17}$$

Finally, the discrete form of the strain energy density is written as:

$$W_{(k)} = \frac{1}{2}\left(\kappa'_{(k)}\Theta^2_{(k)} - \alpha_{(k)}\sum_{j=1}^{N_{\mathcal{H}_k}}\phi_{(k)(j)}\underline{\omega}_{(k)(j)}\underline{e}^{\mathrm{d}}_{(k)(j)}\underline{e}^{\mathrm{d}}_{(k)(j)}V'_{(j)}\right). \tag{18}$$

3.1. Modelling of FGMs

It is well known that the FGMs do not have sharp material interfaces and both thermal and mechanical properties of FGMs are assumed to vary gradually through the width or thickness direction. Considering the fact that the PD parameters have been obtained by assuming the material is homogeneous and bulk (far from the boundary), some simplifications are required to model variable material properties. If a material property varies dramatically within the horizon of a particle, it might be expected that it will induce error in the conventionally obtained PD parameters. By relatively fine discretization with slight or moderate variation of the material properties within the horizon, the localized homogenization approach performs well for the PD modelling of FGMs. In this approach, the fundamental equations remain the same; however, the material parameters for a bond are averaged values of the properties for particles at each end of the bond, which is the simplest but efficient modelling technique for FGMs.

The approach described above has also been widely adopted for FGM modelling within PD perspective [33,42,43]. Recently, some researchers have proposed to implement weighted averaging of the material properties for a bond rather than simple averaging [44,45]. Rahimi et al. [17] proposed a dominance approach, which is similar to the weighted averaging, for evaluating the bond properties in FGMs. Rahimi et al. [17] have established their proposal based on the assumption that the maximum bond force is limited to the resistance of the particle, which has smaller stiffness among the particles at each end of the bond. The softer material property is therefore multiplied by a dominance factor.

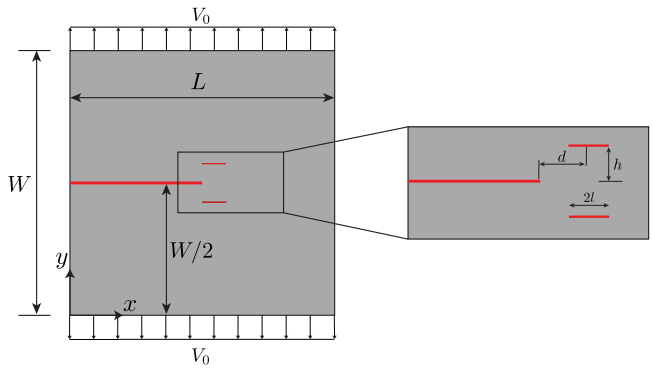

Fig. 2. The benchmark model adopted from Refs. [11,12] (not in true scale).

The present FGM modelling technique is same as the one implemented in our previous work [33]. For calculating the magnitude of force density vector, the PD parameters, α and k' are evaluated by using mean values of the material properties at particles (k) and (j). One should be careful in calculating the parameter α as its denominator is independent of the material properties. The averaging of α parameter is performed as:

$$\alpha_{(k)(j)} = \frac{8(\mu_{(k)} + \mu_{(j)})}{2q_{(k)}}, \tag{19}$$

where $\mu_{(k)}$ and $\mu_{(j)}$ are the shear moduli of the particles at each side of the PD bond. The bond parameter $\kappa'_{(k)(j)}$ is obtained by averaging Poisson's ratio and Elastic modulus of the particles (k) and (j). The parameter β is only function of Poisson's ratio, as it is known from a reference work [46], the influence of Poisson's ratio on the crack propagation is less significant compared to that of elastic modulus and fracture toughness. The Poisson's ratio can be assumed as constant.

For evaluating the strain energy density of the particle (k), pointwise quantities of PD parameters without averaging, $\kappa'_{(k)}$ and $\beta_{(k)}$, and dilatation, $\Theta_{(k)}$, are utilized.

4. Numerical studies

We consider various micro-crack configurations ahead of a main crack to carry out a comprehensive investigation on their influence on the crack growth. Accordingly, we first verify our implementation with a benchmark study for homogeneous materials. In the benchmark case, two parallel micro-cracks, which are aligned with the main crack, are introduced. Then, the crack patterns are compared with the reference works. After successful verification of the present OSB-PD implementation, the FGMs are considered. Co-linear and complex micro-cracks are introduced for FGM specimens under uni-axial tension load for fast crack propagation and three-point bending test scenarios.

4.1. Benchmark study with homogeneous materials

The validation of the present OSB-PD implementation for the micro-crack modelling and simulation is aimed by utilizing a benchmark model, which was studied by Refs. [11,12]. The model is demonstrated in Fig. 2 with a close-up view on the micro-crack zone.

In Fig. 2, entire modelling and material parameters are adopted from Refs. [11,12]. The geometrical parameters are as follows. The aspect ratio of the model is 1.0, i.e., $L = W = 50$ mm. The main crack

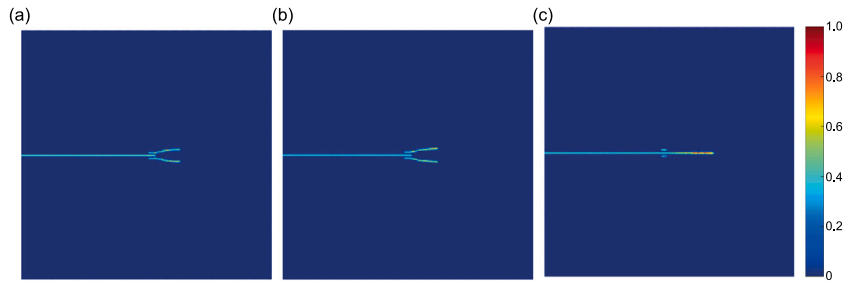

Fig. 3. Damage patterns with local damage parameter (φ) at 1000th step: (a) $s/l = 2$, (b) $s/l = 0$, (c) $s/l = -2$.

length is taken as the half of the length, $L_{\text{main}} = L/2$, and the size of the micro-cracks are assumed as $2l = L/50$. The other parameters related to micro-crack locations are: $h = 1.25l$, and the distance d is varied as $2l$, 0, $-2l$. Here, the negative value of d means that the micro-cracks fall behind the main crack tip.

The material properties are: modulus of elasticity, $E = 2940$ MPa, Poisson's ratio, $\nu = 0.38$, the density, $\rho = 1200$ kg/m^3, and the fracture energy is $G_c = 602$ J/m^2. The critical stretch value for the assessment of the crack propagation is obtained by using Eq. (9).

The model is discretized with a particle distance, $dx = 0.1$ mm, and the horizon size is taken as $\delta = 3.015\times dx$. A constant velocity boundary condition, $V_0 = 5$ m/s is imposed on both top and bottom surfaces of the model by invoking fictitious material layers, whose width is $3\times dx$.

In performing explicit time integration, proper determination of the critical time step size is crucial. Silling and Askari [27] proposed a critical time step size criterion in the PD perspective. In the present work, the time step size is chosen as $dt = 4\times 10^{-8}$ s, which is consistent with Refs. [11,12] as well as meets the criterion proposed by Silling and Askari [27]. Total number of steps is taken as $nt = 2000$.

Damage patterns for the homogeneous model were provided for the 1000th step in Refs. [11,12]. For the comparison purpose, the damage patterns are provided for the same instance, i.e., 1000th step in Fig. 3. The damage patterns are considered to be in a very good agreement with the reported ones in Refs. [11,12]. Please see Fig. 9 in Ref. [12] for the comparison. The crack propagation starts around 500th time step for all cases, which is also consistent with the reported values in Refs. [11]. These results also indicate that the Poisson's ratio is not a main governing parameter of the crack propagation, since it is adopted as $\nu = 0.38$ in the present work, while the reference works [11,12] utilized bond-based PD with a fixed Poisson's ratio, $\nu = 1/3$.

4.2. Fast crack propagation scenarios under tension loading

Fast crack propagation in FGMs was studied by bond-based PD in [43]. Then, the same specimens have been adopted by the present authors [33] and a thorough investigation of crack propagation has been carried out by utilizing OSB-PD formulation. Ref. [33] reported that the crack propagation speed reaches the critical wave speed, which is around $0.6C_T$ and branching takes place. C_T represents the transverse wave speed in solids, see Ref. [33]. In the present study, same specimens are adopted and various micro-crack configurations are introduced ahead of the main crack tip. The main dimensions of the specimen, shown in Fig. 4, are as follows. The length is $L = 0.1$ m and the width is $W = 0.04$ m. The main crack length is $L_{\text{main}} = L/2$. The loading condition is also assumed to be same as the previous works [33,43]; symmetrical tension load, with a magnitude of $\sigma_0 = 15$ MPa is suddenly applied on both top and bottom edges.

The material parameters are assumed to be same as the previous works [33,43]. As demonstrated in Fig. 4, the material stiffness as well as the density increases from bottom to top surface. In accordance with the reference works [33,43], linear variations for the material properties are considered as:

$$K_{\text{IC}}(y) = 2.1 + \frac{3.6 - 2.1}{40}y, \tag{20}$$

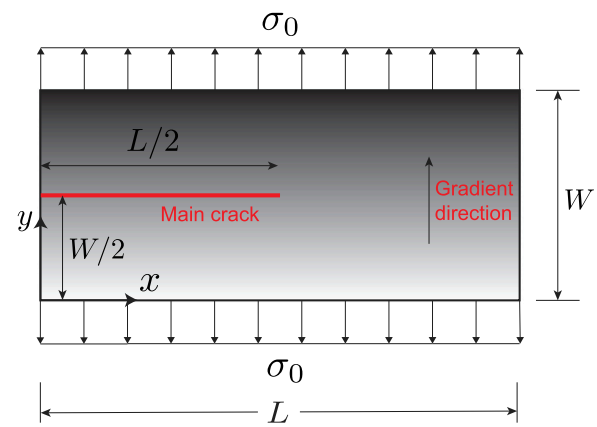

Fig. 4. Representative model of FGM specimens for fast crack propagation.

$$E(y) = 3.8 + \frac{11.1 - 3.8}{40}y, \tag{21}$$

$$\rho(y) = 918 + \frac{1812 - 918}{40}y. \tag{22}$$

In the above equations, y is varied between 0 and 40 mm. The units for fracture toughness, elastic modulus and mass density are MPa m$^{1/2}$, GPa and kg/m^3, respectively. The plane stress condition is adopted for this problem, and the Poisson's ratio is considered as constant, $\nu = 1/3$.

The critical stretch for a bond is evaluated by taking the mean values of the material properties. The critical energy release rate is computed for each particle as:

$$G_c(y) = \frac{K_{\text{IC}}^2(y)}{E(y)}. \tag{23}$$

Then, by using the same simplified approach as described in Section 3.1, the mean value of the critical energy release rates of the particles at each end of the bond is invoked in Eq. (9).

4.2.1. Numerical convergence tests

Although we presented consistent results for the FGMs considering crack growth in our previous paper [33], it would be useful to carry out convergence analyses to determine the optimum discretization size and the horizon parameter. In that sense, we have decided to perform convergence study for the crack growth case of co-linear micro-crack configurations. In the PD simulations, the convergence studies involve two steps [47]: (i) m convergence, in which the horizon parameter is varied for a fixed dx value, (ii) δ convergence, in which the particle discretization is varied for a fixed m value.

In the convergence study, the number of micro-cracks is adopted as two, and the cracks are aligned with the orientation of the main crack as shown in Fig. 5.

The parameters of the micro-cracks are adopted from [11], which are given as follows. The parameter a represents the horizontal distance

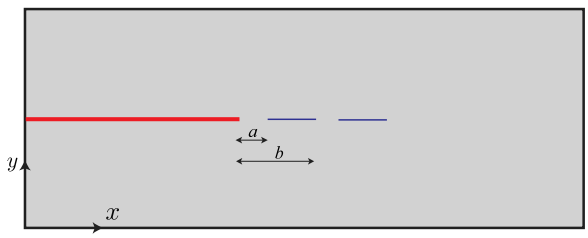

Fig. 5. Co-linear micro-crack configurations for the convergence study.

between the cracks, and taken as $a = L_{\text{main}}/40$. The relationship between the micro-crack size parameters is adopted as $a/b = 0.4$. Then, the size of a micro-crack becomes $b - a = 1.875$ mm.

In order to represent the micro-crack shapes well, the particle distance, dx, is taken as 0.2 mm in the m convergence study. Then, the horizon parameter, m, is varied as 3, 4 and 5. In all horizon parameter cases, the horizon size becomes smaller than the size of a micro-crack. If the horizon size becomes comparably larger than the size of a micro-crack, then the micro-crack cannot be represented as a sharp interface, but as a damage zone. Moreover, the model discretization will affect the critical time step size that is crucial for a stable explicit time integration.

Once the m convergence has been completed, the δ convergence study is performed for the fixed horizon parameter, $m = 4$, varying the particle distance, dx as 0.1, 0.2 and 0.4 mm. For these configurations, $m = 4$ is considered to be an optimum value as the lower value of m may restrict the crack growth path due to the insufficient number of bonds within the horizon; on the other hand, the larger value, i.e., $m = 5$ may reduce the solution accuracy because of the assumptions made for the FGM modelling based on the averaging technique. Based on the guidance from the Refs. [27,37], we have obtained the critical time step sizes. In one case, $m = 4$ with $dx = 0.1$ mm, we adopt $\Delta t = 30 \times 10^{-9}$ s. As for the other cases, $\Delta t = 50 \times 10^{-9}$ s guarantees a stable explicit time integration.

We have performed the convergence study based on the parameters we mentioned earlier, and the crack patterns after 60 μs with the local damage parameter (φ) map are provided in Fig. 6. This figure indicates that larger horizon sizes, i.e., $m = 5$ in the m convergence and $dx = 0.4$ mm in δ convergence, cannot capture the local branching due to the presence of the micro-cracks. The final crack patterns obtained by these parameters are almost the same with damage patterns without micro-crack cases. Based on the experiences from our previous work [33] as well as the findings from [43], we may expect two main branches with multiple local branches. This behaviour was captured well in case of $m = 4$ with $dx = 0.1$ and 0.2 mm. Although $dx = 0.1$ mm with $m = 4$ case represents the sharp crack faces with high accuracy, its computational efficiency is extremely lower compared to the case $dx = 0.2$ mm with $m = 4$.

In the convergence study, we have also examined the onset of crack propagation and the final location of the crack tip when the simulations end. It was found that the main crack starts to grow between 12 and 13 μs, which suggests that the influence of setted parameters on the instance of the crack propagation is just marginal.

The x-coordinate of the crack tips at the end of the simulation, i.e., 60 μs, were recorded and it was found that they may show slight variation depending upon the horizon sizes from 81.0 to 86.0 mm for the smallest ($m = 4$ and $dx = 0.1$ mm) and largest ($m = 4$ and $dx = 0.4$ mm) horizon sizes, respectively.

The findings from the convergence study suggest that the discretization with $m = 4$ and $dx = 0.2$ mm seems to be the most optimum model that gives accurate results with affordable computational expenses.

4.2.2. Co-linear micro-crack configurations

The optimum discretization parameters along with the stable time step sizes have been identified in the convergence study. So, we discretize the model with $m = 4$ and $dx = 0.2$ mm parameters. The time step size is taken as $\Delta t = 50 \times 10^{-9}$ s. The dimensions of the micro-cracks and their spacing are same as the convergence study. The model parameters are schematically given in Fig. 7(a), while Fig. 7(b) shows the numerical PD models.

The orientation of the micro-cracks is expressed with respect to horizontal axis. In regular configuration, the micro-crack is aligned with the main crack, and the crack orientation, θ, becomes 0°. For the angular micro-crack configurations, θ is varied as 45°, 90° and 135°. Furthermore, number of micro-cracks are varied as $nc = 1, 2, 4$. Their influence on the propagation of the main crack is examined by comparing horizontal locations of the crack tips for different configurations and final damage patterns.

Fig. 8 illustrates the x-coordinates of the crack tip locations during the simulation. One of the main inference from the given figure is that if the micro-cracks are aligned with the main crack, the crack tip jumps through micro-cracks and travels longer distance within the considered time interval. Despite the slopes of the given curves follow a similar trend, earlier onset of crack propagation for $\theta = 0°$ case is the main reason for the longer travel distance. On the other hand, as it is expected, the micro-cracks orthogonal to the main crack face ($\theta = 90°$) retard the onset of crack propagation, which in turn a less distance is travelled by the main crack. It must be noted that the influence of orthogonal micro-cracks is just marginal on the final crack tip position regardless of the number of micro-cracks. The effects of diagonal micro-cracks ($\theta = 45°, 135°$) are almost the same on the location of the crack tip within the given time interval. These configurations cause slightly earlier onset of the crack propagation compared to the only main crack case.

Effects of co-linear micro-cracks can also be discussed based on the crack paths at the end of the simulations. Accordingly, the damage patterns for the various micro-crack configuration cases as well as the only main crack case are provided in Fig. 9

The impact of the micro-cracks might be judged by the branching behaviour of the main crack. Crack branching is associated with the local crack speed that reaches the critical wave speed ($0.6C_T$) [48,49]. This phenomenon was studied extensively in the previous work of the authors [33]. As it is seen in Fig. 9, obvious single crack branching, similar to that of only main crack case, occurs in a few cases. In $nc = 1$ case, the crack patterns are mostly similar to that of the only main crack case, which shows the limited impact of the micro-cracks. However, in some cases; particularly, $nc = 4$ case with $\theta = 45°, 90°$ and 135°, there is no obvious branching unlike the only main crack case, which means that the crack does not have sufficient energy to completely branch. In the damage patterns for these cases, one can observe local small-branching and accumulated damage rather than a sharp crack face.

4.2.3. Complex micro-crack patterns

The micro-crack configurations studied so far have limited influence on the crack growth and they may play an accelerating role in some configurations, i.e., co-linear micro-cracks with $\theta = 0°$. In this section, we therefore consider complex micro-crack configurations that possibly have some toughening effects. Basoglu et al. [12] examined the toughening mechanisms of the various micro-crack configurations in the homogeneous materials. They also reported that the crescent-like micro-cracks are the most effective configuration in suppressing the crack propagation speed among the numerical examples considered in their study. Recently, the crescent-like micro-cracks in regular and random patterns were also numerically implemented in Kalthoff-Winkler impact tests by Candas et al. [50]. Even if the efficiency of this configuration has been proven for homogeneous materials, its toughening effect has to be studied for FGMs. In the present work, we

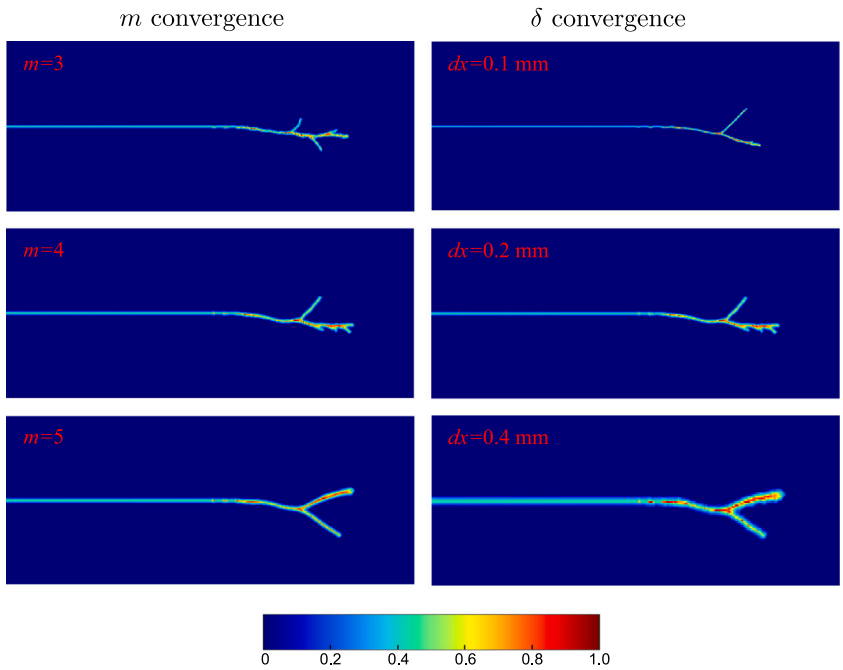

Fig. 6. The damage patterns after 60 μs.

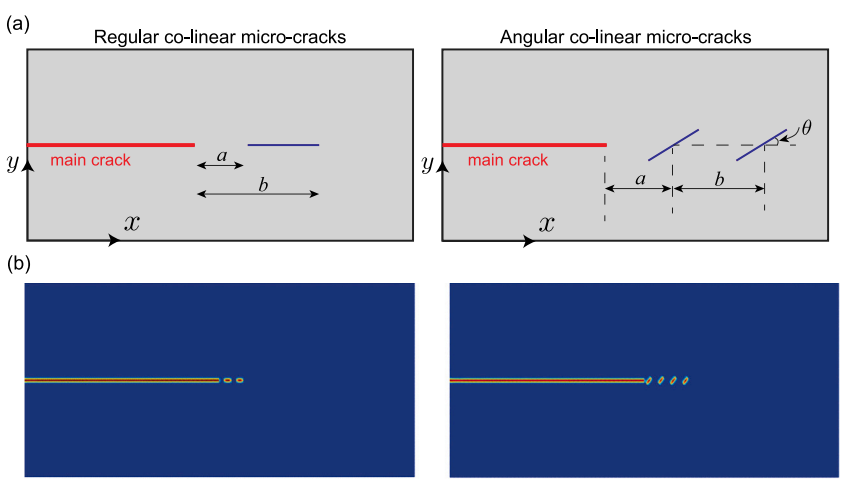

Fig. 7. Co-linear micro-crack configurations: (a) schematic illustrations (not in true scale), (b) numerical PD models.

therefore adopt crescent-like micro-cracks, curved cracks and orbited micro-cracks ahead of the main-crack tip in FGMs. The modelling parameters are demonstrated on the numerical models with close-up views in Fig. 10.

In the crescent-like configurations, see Fig. 10(a), three arrays of micro-cracks in arch shape are invoked. The first array involves seven micro-cracks; eight and nine micro-cracks constitute the second and third micro-crack arrays, respectively. Origin of the arc shape of the crack arrays is allocated slightly behind the main crack tip, and radius for the first array is r_{in} = 7.5 mm. The distance between the main crack tip and the first crack array is 5.0 mm. The crescent-like micro-cracks have the size, a = 2.0 mm, and this value is the offset distance between the crack arrays as well. The offset angle between the micro-cracks in the same array is set as 20°.

Fig. 10(b) demonstrates a curved crack that acts as a shield for the tip of the main crack. The centre of the curved crack is located at the tip of the main crack with a radius, r_{in} = 7.5 mm. The sweep angle of the curved crack is 240°.

The orbited micro-cracks in Fig. 10(c) have the same properties with the crescent-like micro-cracks in terms of the orbit radius and the crack offset angle. The micro-crack size is adopted as a = 2.5 mm, which is the offset distance between the crack arrays as well. In this configuration, there are five layers, and the number of micro-cracks are increasing from one to five as the orbit circle enlarges.

The crack tip locations in the horizontal direction have been captured and presented in Fig. 11. This figure suggests that the crescent-like and orbited micro-cracks have similar effects on the crack growth as expected; however, the final horizontal location of the crack tip in case of crescent-like micro-cracks is slightly smaller than that of orbited micro-cracks case. On the other hand, the curved crack retards the onset of crack growth significantly owing the its continuous geometry and shielding effect. When the crack starts to propagate, the crack growth rate is the smallest among others, see the slope of curve within the interval of 15–22 μs. Beyond 22 μs, the crack tip suddenly jumps as it is shown in Fig. 12(b). The crack growth takes place on the back side of the curved crack in addition to main crack. In this case, we have considered the right-most crack tip as the new crack tip.

Fig. 12(a) sheds light on the almost flat-region of the crack-growth rate in 30–35 μs interval for the crescent-like micro-crack case. In

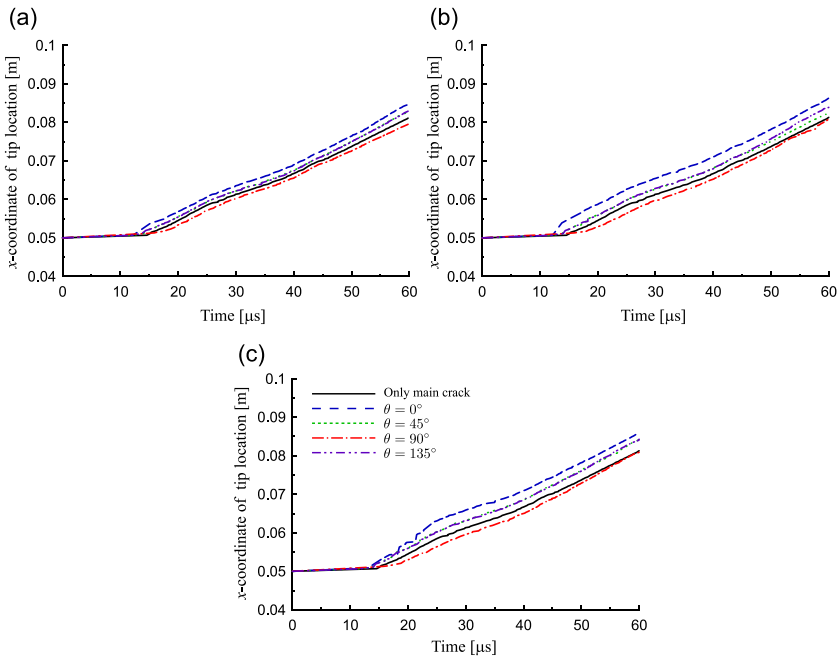

Fig. 8. Advance of crack tips in the horizontal direction for co-linear micro-crack configurations: (a) $nc = 1$, (b) $nc = 2$, (c) $nc = 4$.

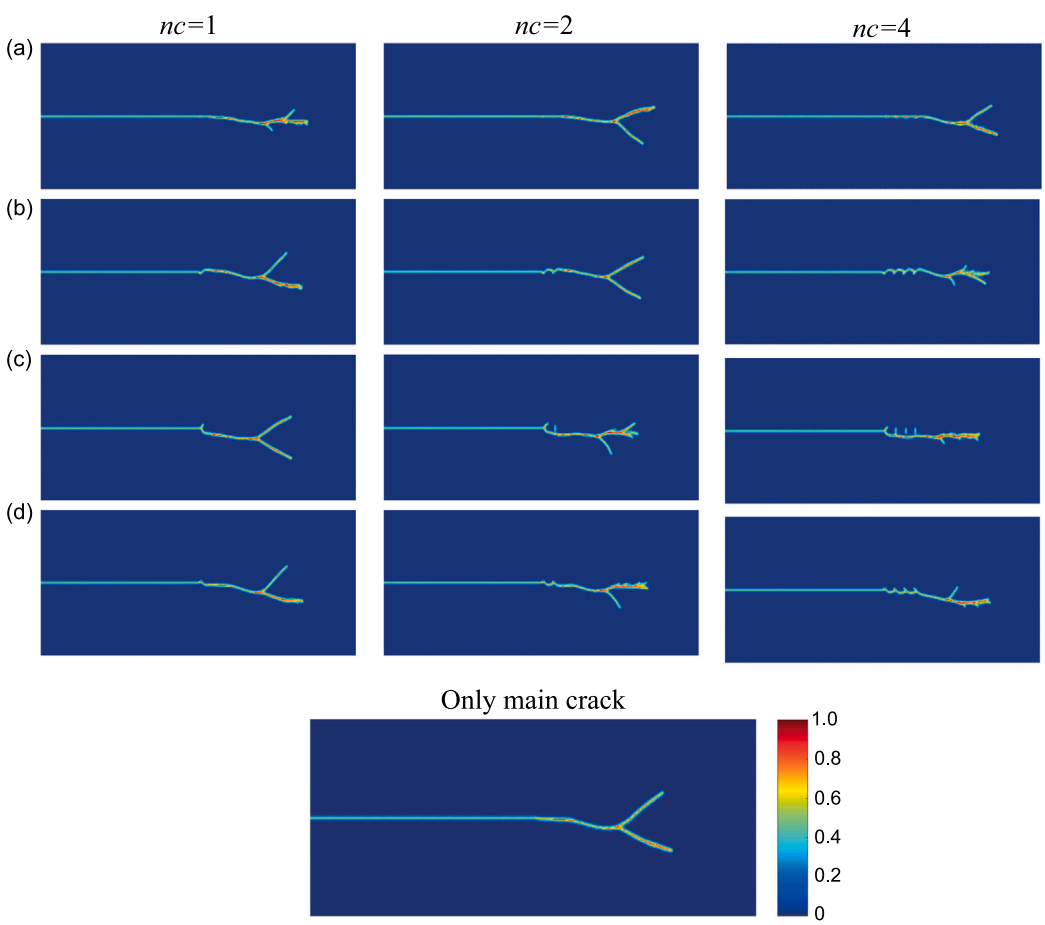

Fig. 9. Damage patterns with local damage parameter (φ) for co-linear micro-crack configuration cases: (a) $\theta = 0°$, (b) $\theta = 45°$, (c) $\theta = 90°$, (d) $\theta = 135°$.

this interval, main crack reaches the micro-crack cluster; afterwards, it splits into multiple branches because of the multiple stress concentrations at the tips of the micro-cracks. We can interpret locations of the stress concentrations as well as their magnitudes in terms strain energy densities calculated by Eq. (18). The strain energy distributions for both with and without micro-cracks cases at $t = 14$ μs are demonstrated in Fig. 13.

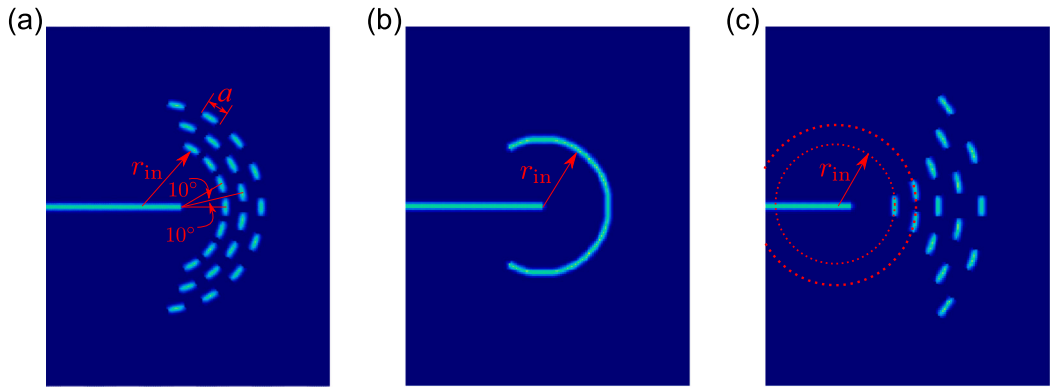

Fig. 10. Modelling of complex micro-crack configurations: (a) crescent-like, (b) curved, (c) orbited micro-cracks.

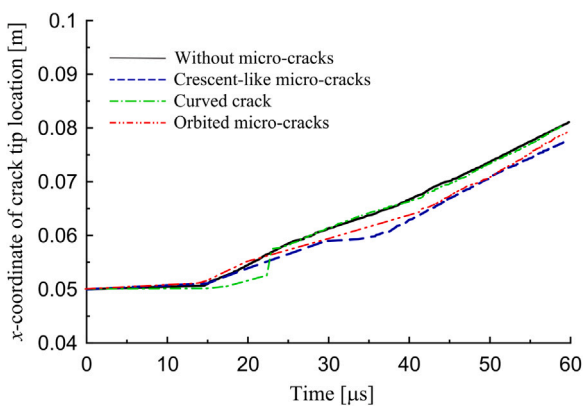

Fig. 11. Crack tip locations in the horizontal axis with respect to time.

As it is apparent in Fig. 13, the maximum strain energy density takes place in the only main crack case. Although the maximum values of strain energy densities for the crescent-like and orbited micro-crack cases are slightly lower than the only main crack case, their values double the maximum strain energy density value of the curved crack case. It is worth noting that the maximum strain energy density develops at the lower tip of the curved crack, while the most stressed locations are the main crack tips for other cases. Moreover, the back side of the curved crack is also stressed noticeably. The strain energy plots confirm the crack-tip location histories in Fig. 11. Due to the lower strain energy density at the tip of the main crack in curved crack case, the growth starts late; what is more, the growth rate is the smallest until a certain point. From that point, a new crack initiates from the back side of the curved crack, see Fig. 12(b). Then, the new crack propagates almost in the same rate with the only main crack case, see Fig. 11. Considering the findings above, the most efficient way to suppress the crack growth rate seems to be the crescent-like micro-crack configuration as its final crack-tip coordinate is the smallest. On the other hand, from the practical point of view, the curved crack case is the most efficient way for retarding onset of the crack propagation.

4.3. Three-point bending (TPB) test scenarios with micro-cracks

The fast crack propagation scenarios for various micro-crack configurations have been studied thus far in Section 4.2. The crack branching has been therefore observed in many of the considered cases. Next, we are going to replicate TPB test specimens including micro-cracks in the OSB-PD framework. TPB test setup mostly yields lower crack propagation speed without any crack branching. This test configuration was studied by Cheng et al. [42] by utilizing the bond-based PD formulation. Then, the present authors conducted a thorough investigation of the same problem by the OSB-PD formulation for only main crack cases [33]. In that study, we reported mixed-mode crack propagation without any branching. The TPB test model with the main dimensions and loading condition is given in Fig. 14.

Fig. 14(a) shows the model without micro-cracks. The main crack is located on the stiff side of the specimen. The bottom supports are modelled in terms of reacting opposite loads. The main loading is applied on the top surface with a distance from the mid-span, see Fig. 14(a). The length of the loaded part is 6.0 mm. Each of the support loadings is acting on a 3.0 mm distance at the bottom surface. These parameters are all consistent with the reference works [33,42]. Unlike the reference works, only one loading condition, called rump-up-down loading, as defined in Fig. 14(b) is considered.

The material properties are assumed to be varying linearly from bottom to top surface, which is also a consistent assumption with the reference works [33,42]. The variation of the material properties through the width of the model can be expressed as follows.

$$K_{IC}(y) = 2.2 - \frac{2.2 - 1.4}{43} y, \tag{24}$$

$$E(y) = 10 - \frac{10 - 4}{43} y, \tag{25}$$

$$\rho(y) = 1750 - \frac{1750 - 1175}{43} y, \tag{26}$$

where y is varied between 0 and 43 mm. The units for fracture toughness, elastic modulus and mass density are MPa $m^{1/2}$, GPa and kg/m^3, respectively. Poisson's ratio is considered to be constant as $\nu = 0.34$. Critical energy release rate is obtained by Eq. (23) in a point-wise manner, and the bond properties are obtained in the same manner with the fast crack propagation scenarios in Section 4.2.

The model is discretized with a particle distance of $dx = 0.2$ mm, and the horizon size is set as $\delta = 4 \times dx$. Critical time step size for a stable explicit time integration is taken same as the reference works, $\Delta t = 20 \times 10^{-9}$ s. The total simulation time is adopted as 300 μs to ensure full failure of the specimens.

4.3.1. Co-linear micro-crack configurations

We consider co-linear micro-crack configurations first. The modelling and parameters are defined in the same manner with Section 4.2. The TPB models with co-linear micro-cracks are schematically illustrated in Fig. 15(a). The discretized numerical PD models are provided in Fig. 15(b).

In Fig. 15(a), the a/b ratio is taken as 0.4. The distance from the main crack tip to the first micro-crack is $a = L_{main}/8$. The crack orientation angle is expressed with respect to horizontal axis and varied as $\theta = 0°, 45°, 90°$ and 135°. The number of co-linear micro-cracks is considered as $nc = 1, 2$ and 4.

The crack tip locations in the vertical direction have been recorded and presented in Fig. 16. As can be clearly seen in the figure, the

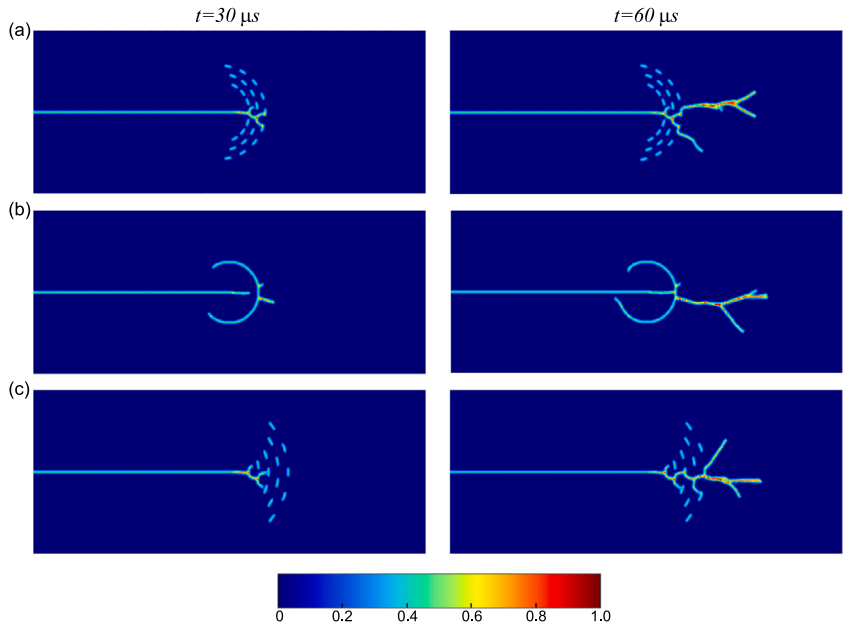

Fig. 12. The damage patterns with local damage parameter (φ) for t = 30 and 60 μs: (a) crescent-like micro-cracks, (b) curved crack, (c) orbited micro-cracks.

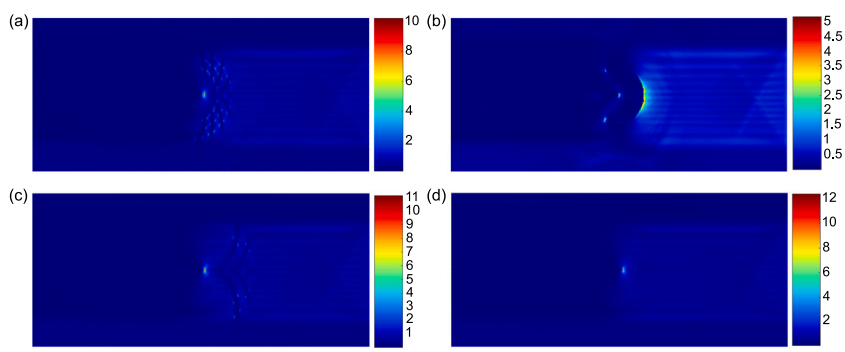

Fig. 13. Strain energy density [J/m^3] distributions (×10^5) at t = 14 μs: (a) crescent-like micro-cracks, (b) curved cracks, (c) orbited cracks, (d) only main crack.

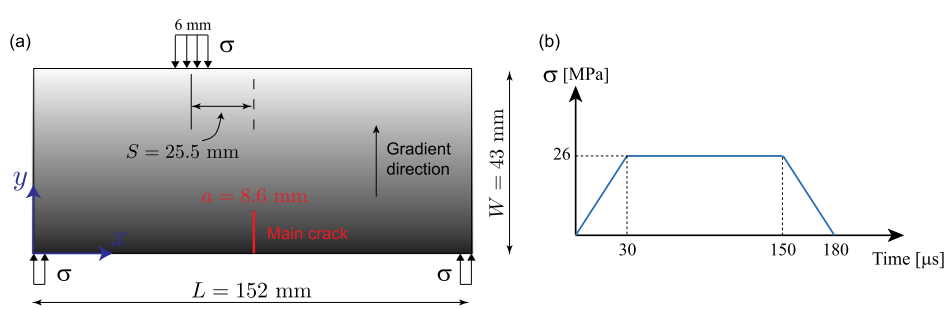

Fig. 14. Representative model of FGM specimens for TPB simulations: (a) main dimensions with problem description, (b) loading condition.

influence of the co-linear micro-cracks on the crack propagation speed is just marginal. The crack propagation starts slightly earlier for $\theta = 90°$ case. However, the crack tip locations become almost the same in the end. Fig. 16 also suggests that the full failure of the specimens takes place in a small time interval between 265–275 μs.

To explain better the impacts of the co-linear micro-cracks, the damage patterns at 250 μs are provided for both only main crack and co-linear micro-crack cases in Fig. 17. As it is seen in the figure, the crack tip locations and the crack paths are very much similar to each other. The only visible impact of the co-linear micro-cracks can be said that the mode-mixity for the crack propagation is suppressed in a certain level. Furthermore, the crack patterns remain simple unlike the fast crack propagation scenarios, which have complicated crack patterns with multiple branching as reported in Section 4.2.

4.3.2. Complex micro-crack patterns

In a similar fashion with the fast crack propagation scenarios, the complex crack patterns are allocated ahead of the main crack tip. The modelling strategy is similar with the fast crack propagation case as shown in Fig. 10. In the curved crack case, the inner radius is adjusted as, r_{in} = 5.0 mm. The size of micro-cracks for both crescent and orbited configurations is utilized as a = 2.0 mm.

The crack tip locations in the vertical direction were captured and presented in Fig. 18. This figure suggests that only distinguishable

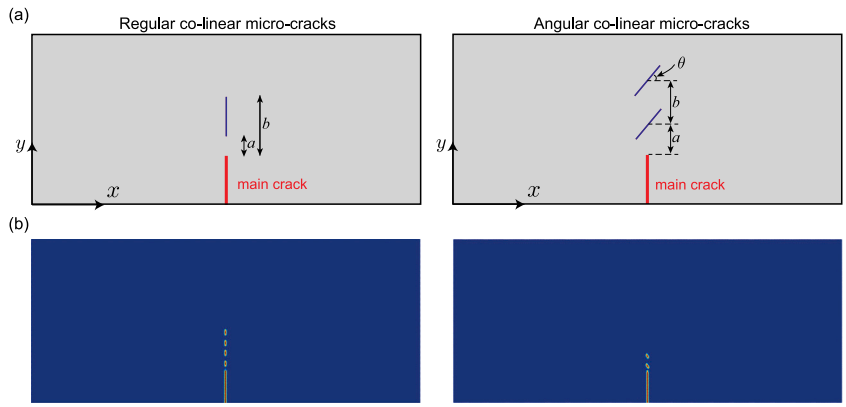

Fig. 15. Co-linear micro-crack configurations for TPB models: (a) schematic illustrations (not in true scale), (b) numerical PD models.

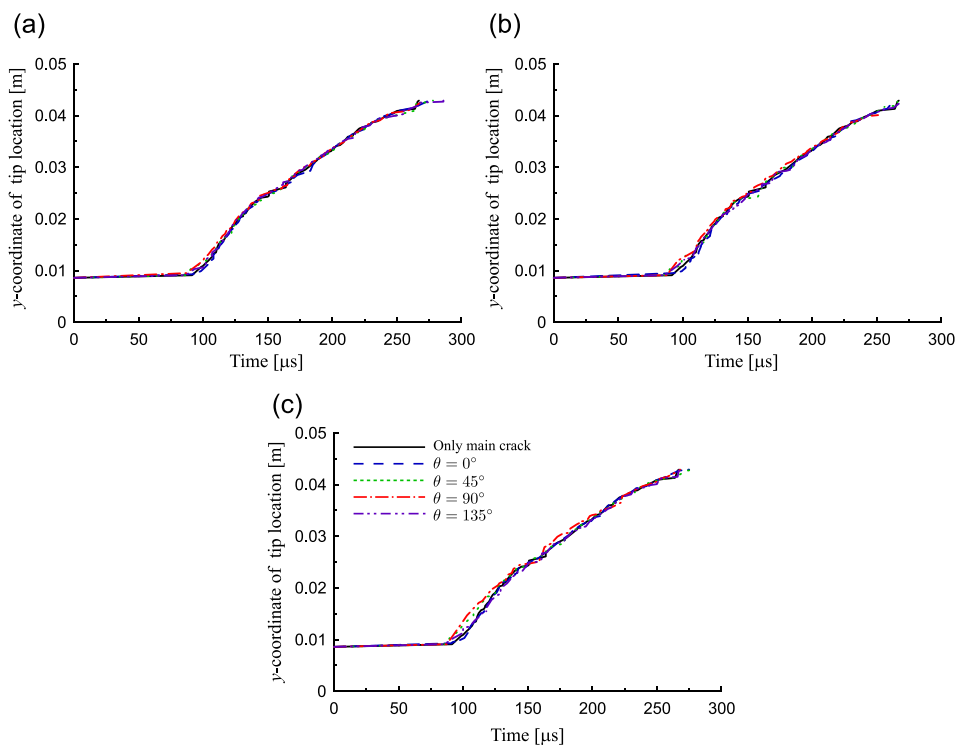

Fig. 16. Advance of crack tips in vertical direction for co-linear micro-crack configurations: (a) $nc = 1$, (b) $nc = 2$, (c) $nc = 4$.

impact is observed for the curved crack case. The other micro-crack configurations demonstrate more or less the same crack growth rate with small local oscillations, whereas the curved crack plays a significant shield role for the main crack, and suppresses its propagation rate, see the slope of the curve for the curved crack case in Fig. 18.

The main crack grows with a smaller rate between 100–150 μs in the curved crack case. Then, the tip location suddenly jumps because of the initiation of new cracks on the back side of the curved crack, see Fig. 19(b). Afterwards, the growth rate for all cases follows a similar trend. Fig. 18 shows that the final failure of the specimens takes place between 260–275 μs for all cases except the curved crack configuration. In this case, the full failure of the specimen occurs around 297 μs. The damage patterns for the TPB specimens involving various micro-crack configurations are provided for $t = 150$ and 250 μs in Fig. 19. The given damage patterns for the instance of $t = 250$ in Fig. 19 indicate that the crescent like micro-cracks cannot suppress the mode mixity of the main crack. The final crack path is obviously a mixed-mode fracture for crescent-like configuration, while the orbited micro-cracks are able to suppress the mixed-mode fracture to a some extent compared to the case of crescent-like micro-cracks. As for the curved crack case, we observe almost mode-I fracture with insignificant level of horizontal crack deflection.

The crack growth rates as well as the onset of the crack propagation can be interpreted from the strain energy density plots. In a similar fashion with the fast crack propagation scenarios, the strain energy density of the specimens with and without micro-cracks are presented in Fig. 20. This figure suggests that the strain energy densities for the only main crack and with micro-cracks are in the same order except the curved crack case at $t = 90$ μs. In all cases, the maximum value of the strain energy density occurs at the main crack tip prior to onset of crack growth. However, the strain energy concentration on the right-hand side tip of the curved crack can be noticed, see Fig. 20(b). Furthermore,

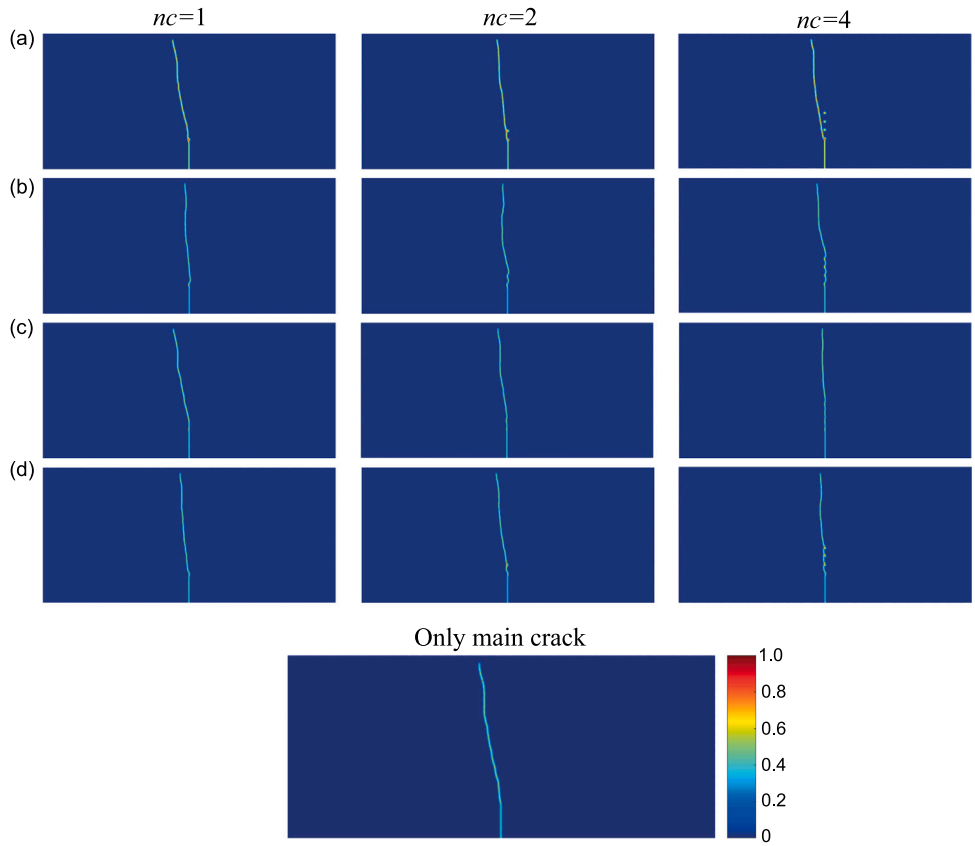

Fig. 17. Damage patterns with local damage parameter (φ) for co-linear micro-crack configurations at $t = 250$ μs: (a) $\theta = 0°$, (b) $\theta = 45°$, (c) $\theta = 90°$, (d) $\theta = 135°$.

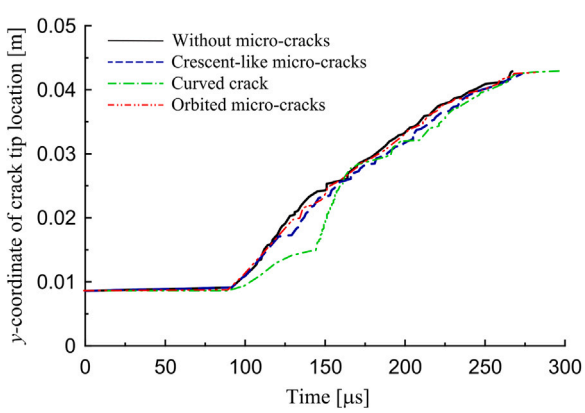

Fig. 18. y-coordinate of crack tip locations with respect to time.

a slightly stressed region on the back side of the curved crack can be observed in the same plot, which will later cause the crack forming from that region.

The forming of the new crack tip from the back side of the curved crack can be explained as follows. At the initial stage of the crack propagation, the most stressed location is the main crack tip. However, as the main crack grows, the strain energy at the tip is released, which results in the decline of the crack growth rate between 100–150 μs, see Fig. 18. At a certain point, the strain energy density at the main crack tip becomes smaller than the strain energy density on the back side of the curved crack. From that point, a new crack starts to grow from the back side. Fig. 20(e) approves that statement as the strain energy density on the back side of the curved crack is much higher than that of the main crack tip at $t = 140$ μs.

5. Conclusions

A comprehensive investigation on the macro–micro crack interactions in FGMs has been carried out employing OSB-PD formulation. Firstly, our micro-crack implementation has been validated by numerical examples for homogeneous materials from the literature. Once the present implementation and modelling have yielded good agreement with the reference results, we proceeded to the FGM implementations. Two different scenarios, namely, fast crack propagation and TPB tests have been considered. In these test set-ups, numerous co-linear and complex micro-crack configurations, i.e., crescent-like and orbited micro cracks, and curved cracks, have been adopted. Co-linear micro-cracks have played an accelerating role for the crack propagation except for one case of $\theta = 90°$ in the fast crack propagation scenarios. The curved crack case retards the onset of crack propagation. On the other hand, a new crack forms from the back side of the curved crack, which follows a similar growth rate with the only-main crack case. The crack growth in the crescent-like and orbited micro-crack cases shows similar behaviour. In case of TPB models, the impact of the co-linear micro-cracks is insignificant in terms of the crack growth rate and the final damage patterns. The same is true for the crescent-like and orbited micro-crack cases; however, the curved crack retards the onset of crack propagation noticeably. Moreover, the time until the full failure is larger for the curved crack configuration. In summary, introducing micro-cracks has improved the toughness when the crack velocity is higher. On the other hand, micro-cracks improved the toughness just marginally in case of lower crack speeds. The curved crack has improved the toughening effect for both scenarios by retarding the onset of the crack propagation.

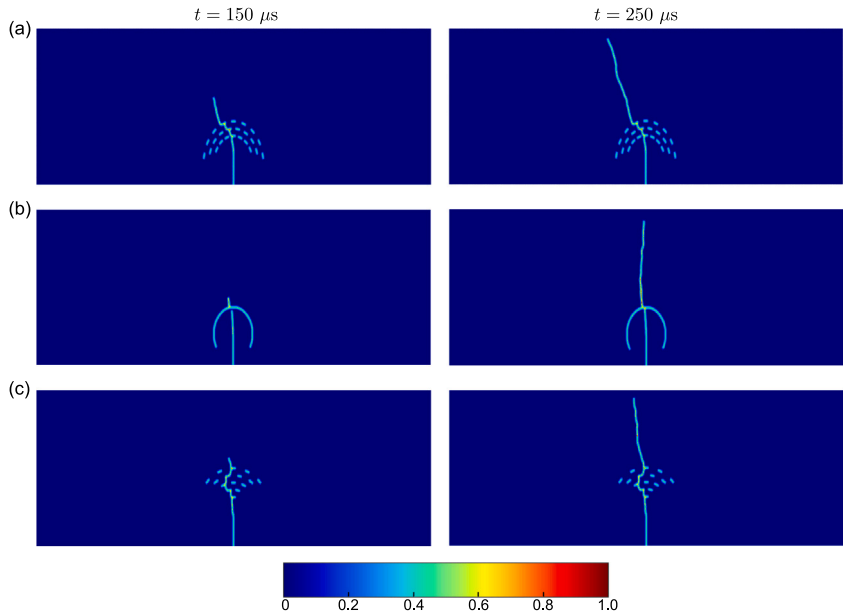

Fig. 19. The damage patterns with local damage parameter (φ) for t = 150 and 250 μs: (a) crescent-like micro-cracks, (b) curved crack, (c) orbited micro-cracks.

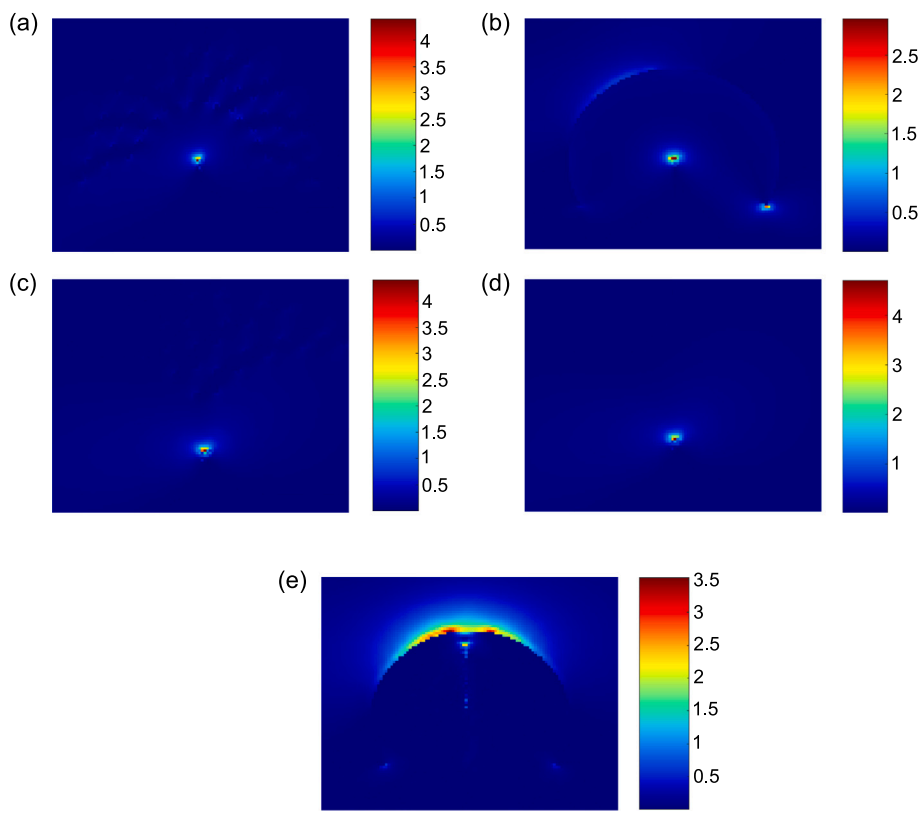

Fig. 20. Close up views of strain energy density [J/m^3] distributions (×10^5): (a) crescent-like micro-cracks at t = 90 μs, (b) curved cracks at t = 90 μs, (c) orbited cracks at t = 90 μs, (d) only main crack at t = 90 μs, (e) curved crack at t = 140 μs.

CRediT authorship contribution statement

M. Ozdemir: Conceptualization, Methodology, Software, Writing – original draft. **M. Imachi:** Methodology, Software. **S. Tanaka:** Supervision, Writing – review & editing. **S. Oterkus:** Supervision, Writing – review & editing. **E. Oterkus:** Supervision, Writing – review & editing.

Declaration of competing interest

The authors declare that they have no known competing financial interests or personal relationships that could have appeared to influence the work reported in this paper.

Data availability

The raw/processed data required to reproduce these findings cannot be shared at this time as the data also forms part of an ongoing study.

Acknowledgement

We would like to acknowledge Dr. Adnan Kefal from Sabanci University, Turkey for the helpful discussions.

References

[1] Thai HT, Kim SE. A review of theories for the modeling and analysis of functionally graded plates and shells. Compos Struct 2015;128:70–86.
[2] Budiansky B, O'Connell RJ. Elastic moduli of a cracked solid. Int J Solid Struct 1976;12:81–97.
[3] Rubinstein AS. Macrocrack interaction with semi-infinite microcrack array. Int J Fract 1985;27:113–9.
[4] Kachanov M. On crack-microcrack interactions. Int J Fract 1986;30:65–72.
[5] Hutchinson JW. Crack tip shielding by micro-cracking in brittle solids. Acta Metall 1987;35(7):1605–19.
[6] Brencich A, Carpinteri A. Stress field interaction and strain energy distribution between a stationary main crack and its process zone. Eng Fract Mech 1998;59(6):797–814.
[7] Petrova V, Tamuzs V, Romalis N. A survey of macro–microcrack interaction problems. Appl Mech Rev 2000;53(5):117–46.
[8] Ducourthial E, Bouchaud E, Chaboche JL. Influence of microcracks on a propagation of macrocracks. Comput Mater Sci 2000;19:229–34.
[9] Feng XQ, Li JY, Ma L, Yu SW. Analysis on interaction of numerous microcracks. Comput Mater Sci 2003;28:454–61.
[10] Zhou T, Huang C, Liu H, Wang J, Zou B, Zhu H. Crack propagation simulation in microstructure of ceramic tool materials. Comput Mater Sci 2021;54:150–6.
[11] Vazic B, Wang H, Diyaroglu C, Oterkus S, Oterkus E. Dynamic propagation of a macrocrack interacting with parallel small cracks. AIMS Mater Sci 2017;4(1):118–36.
[12] Basoglu MF, Zerin Z, Kefal A, Oterkus E. A computational model of peridynamic theory for deflecting behavior of crack propagation with micro-cracks. Comput Mater Sci 2019;162:33–46.
[13] Miyagawa H, Nisitani H. Retardation of fatigue crack propagation due to additional holes or indentations in plate specimens. Bull JSME 1985;28(244):2219–23.
[14] Bleyer J, Roux-Langlois C, Molinari JF. Dynamic crack propagation with a variational phase-field model: limiting speed, crack branching and velocity-toughening mechanisms. Int J Fract 2017;204:79–100.
[15] Rahimi MN, Kefal A, Yildiz M, Oterkus E. An ordinary state-based peridynamic model for toughness enhancement of brittle materials through drilling stop-holes. Comput Mater Sci 2020;182:105773.
[16] Karpenko O, Oterkus S, Oterkus E. Influence of different types of small-size defects on propagation of macro-cracks in brittle materials. J Peridyn Nonlocal Model 2020;2:289–316.
[17] Rahimi MN, Kefal A, Yildiz M. An improved ordinary-state based peridynamic formulation for modeling FGMs with sharp interface transitions. Int J Mech Sci 2021;197:106322.
[18] Budyn É, Zi G, Moës N, Belytschko T. A method for multiple crack growth in brittle materials without remeshing. Internat J Numer Methods Engrg 2004;61:1741–70.
[19] Loehnert S, Belytschko T. Crack shielding and amplification due to multiple microcracks interacting with a macrocrack. Int J Fract 2007;145:1–8.
[20] Wang H, Liu Z, Xu D, Zeng Q, Zhuang Z. Extended finite element method analysis for shielding and amplification effect of a main crack interacted with a group of nearby parallel microcracks. Int J Damage Mech 2016;25(1):4–25.
[21] Bhardwaj G, Singh IV, Mishra BK, Bui TQ. Numerical simulation of functionally graded cracked plates using NURBS based XIGA under different loads and boundary conditions. Compos Struct 2015;126:347–59.
[22] Singh SK, Singh IV, Mishra BK, Bhardwaj G. Analysis of cracked functionally graded material plates using XIGA based on generalized higher-order shear deformation theory. Compos Struct 2019;225:111038.
[23] Bhardwaj G, Singh SK, Patil RU, Godara RK, Khanna K. Thermo-elastic analysis of cracked functionally graded materials using XIGA. Theor Appl Fract Mech 2021;114:103016.
[24] Bhardwaj G, Godara RK, Khanna K, Patil RU. A semi-homogenized extended isogeometric analysis approach for fracture in functionally graded materials containing discontinuities. Proc IME C J Mech Eng Sci 2020;234:2211–32.
[25] Soni A, Grove N, Bhardwaj G, Singh BN. Non-polynomial framework for static analysis of functionally graded carbon nano-tube reinforced plates. Compos Struct 2020;233:111569.
[26] Silling SA. Reformulation of elasticity theory for discontinuities and long-range forces. J Mech Phys Solid 2000;48:175–209.
[27] Silling SA, Askari E. A meshfree method based on the peridynamic model of solid mechanics. Comput Struct 2005;83:1526–35.
[28] Silling SA, Epton M, Weckner O, Xu J, Askari E. Peridynamic states and constitutive modeling. J Elast 2007;88:151–84.
[29] Le QV, Chan WK, Schwartz J. A two-dimensional ordinary, state-based peridynamic model for linearly elastic solids. Internat J Numer Methods Engrg 2014;98:547–61.
[30] Imachi M, Tanaka S, Bui TQ. Mixed-mode dynamic stress intensity factors evaluation using ordinary state-based peridynamics. Theor Appl Fract Mech 2018;93:97–104.
[31] Imachi M, Tanaka S, Bui TQ, Oterkus S, Oterkus E. A computational approach based on ordinary state-based peridynamics with new transition bond for dynamic fracture analysis. Eng Fract Mech 2019;206:359–74.
[32] Imachi M, Tanaka S, Ozdemir M, Bui TQ, Oterkus S, Oterkus E. Dynamic crack arrest analysis by ordinary state-based peridynamics. Int J Fract 2020;221:155–69.
[33] Ozdemir M, Kefal A, Imachi M, Tanaka S, Oterkus E. Dynamic fracture analysis of functionally graded materials using ordinary state-based peridynamics. Compos Struct 2020;244:112296.
[34] Imachi M, Takei T, Ozdemir M, Tanaka S, Oterkus S, Oterkus E. A smoothed variable horizon peridynamics and its application to the fracture parameters evaluation. Acta Mech 2021;232:533–53.
[35] Le QV, Bobaru F. Surface corrections for peridynamic models in elasticity and fracture. Comput Mech 2018;61:499–518.
[36] Dipasquale D, Sarego G, Zaccariotto M, Galvanetto U. A discussion on failure criteria for ordinary state-based peridynamics. Eng Fract Mech 2017;186:378–98.
[37] Madenci E, Oterkus E. Peridynamic theory and its applications. USA: Springer; 2013.
[38] Foster JT, Silling SA, Chen W. An energy based failure criterion for use with peridynamic states. J Multiscale Comput Eng 2011;9(6):675–87.
[39] Karpenko O, Oterkus S, Oterkus E. An in-depth investigation of critical stretch based failure criterion in ordinary state-based peridynamics. Int J Fract 2020;226:97–119.
[40] Chen Z, Niazi S, Bobaru F. A peridynamic model for brittle damage and fracture in porous materials. Int J Rock Mech Min Sci 2019;122:104059.
[41] Ozdemir M, Oterkus S, Oterkus E, Amin I, Nguyen CT, Tanaka S, et al. Evaluation of dynamic behaviour of porous media including micro-cracks by ordinary state-based peridynamics. Eng Comput 2021. http://dx.doi.org/10.1007/s00366-021-01506-4.
[42] Cheng Z, Zhang G, Wang Y, Bobaru F. A peridynamic model for dynamic fracture in functionally graded materials. Compos Struct 2015;133:529–46.
[43] Cheng Z, Liu Y, Zhao J, Feng H, Wu Y. Numerical simulation of crack propagation and branching in functionally graded materials using peridynamic modeling. Eng Fract Mech 2018;191:13–32.
[44] Cheng ZQ, Sui ZB, Yin H, Yuan CF, Chu LS. Studies of dynamic fracture in functionally graded materials using peridynamic modeling with composite weighted bond. Theor Appl Fract Mech 2019;103:102242.
[45] Cheng Z, Sui Z, Yin H, Feng H. Numerical simulation of dynamic fracture in functionally graded materials using peridynamic modeling with composite weighted bonds. Eng Anal Bound Elem 2019;105:31–46.
[46] Delale F, Erdogan F. The crack problem for a nonhomogeneous plane. ASME J Appl Mech 1983;50:609–14.
[47] Bobaru F, Yang M, Alves LF, Silling SA, Askari E, Xu J. Convergence, adaptive refinement, and scaling in 1D peridynamics. Internat J Numer Methods Engrg 2009;77:852–77.
[48] Freund LB. Dynamic fracture mechanics. USA: Cambridge University Press; 1998.
[49] Ravi-Chandar K. Dynamic fracture. USA: Elsevier; 2004.
[50] Candas A, Oterkus E, Imrak CE. Dynamic crack propagation and its interaction with micro-cracks in an impact problem. ASME J Eng Mater Tech 2021;143:011003-1–10.